Analysis and Design of Fault-Tolerant Dual Three-Phase Permanent Magnet Synchronous Machines for eVTOL Applications

1st Yuwen Xu
Department of Mechanical Engineering
University College London
London, UK
yuwen.xu.24@ucl.ac.uk

2nd Shun Cai*
Department of Mechanical Engineering
University College London
London, UK
shun.cai@ucl.ac.uk

3rd Mehdi Baghdadi
Department of Mechanical Engineering
University College London
London, UK
m.baghdadi@ucl.ac.uk

4th Zachary Edwards
Department of Mechanical Engineering
University College London
London, UK
zachary.edwards.24@ucl.ac.uk

5th Zeliang Zhang
Power Electronics and Machines Centre
University of Nottingham
Nottingham, UK
Zeliang.Zhang1@nottingham.ac.uk

6th Guangzhao Luo
Research & Development Institute of Northwestern Polytechnical University
Shenzhen, China
guangzhao.luo@nwpu.edu.cn

***Abstract*—The electric aircraft industry has received an increasing impetus over past decades, driven by the growing attention on environmental sustainability. This paper aims to propose a dual 3-phase fault-tolerant interior permanent magnet synchronous machine (FT-IPMSM) for electric vertical takeoff and landing (eVTOL) applications. Firstly, trade studies were performed on four permanent magnet (PM) configurations with considerations of high-torque-density and high reliability. Then, the multi-physics evaluation is undertaken on a 48-slot/8-pole FT-IPMSM with 2-layer V-shaped PM, during which the thermal viability and mechanical challenges are addressed from design aspects. The results demonstrate the mechanical performance of the machine can be improved by carefully optimizing the rotor structure. This paper also attempts to evaluate the fault-tolerance of the prototype with two different dual 3-phase winding configurations. It verifies that the proposed segregated dual 3-phase winding has comparable performance to the conventional design under both healthy and open-circuit (OC) fault, while the segregated winding has superior short-circuit (SC) fault currents and output torque under the SC condition.**

Keywords—Dual 3-phase winding, interior permanent magnet synchronous machines, optimization, multi-physics performance, fault-tolerant capabilities

I. INTRODUCTION

Air transport has grown increasingly popular in recent years, resulting in a significant rise in greenhouse gas emissions. It is expected that there will be around 2800 million tonnes of CO_2 emissions and 620Mt fossil fuel consumption by 2050 [1] [2]. With ever-growing concerns about environmental pollution, aircraft electrification, such as electrical vertical takeoff and landing (eVTOL) technologies, combined with high performance electrified propulsion systems has emerged as a highly promising research area [3].

The application of electrified propulsion systems in aircraft necessitates the replacement of conventional hydraulic, pneumatic, and mechanical components with electric machines, which are supposed to be of high torque and high power [4] [5]. Permanent magnet (PM) synchronous machines have become a focal point due to their superior output performance and efficiency [6]. The integration of PM machines into electrified propulsion systems can eliminate gear boxes and internal combustion engines, thereby reducing the mechanical complexity and fossil energy consumption. These advancements lead to a reduction in acoustic noise and vibration, resulting in improved system efficiency and passenger comfort.

In addition, high reliability is of high importance for the commercial aviation industry, where passenger safety is paramount. The interior permanent magnet synchronous machine (IPMSM) demonstrates better PM utilization compared to the surface-mounted counterpart, as it can employ the reluctance torque due to the inconsistency of the *d*-axis and *q*-axis reluctance [7]-[10]. The existence of reluctance torque allows the machine to maintain the output capability with a reduced PM volume, which is beneficial for the restriction of the short-circuit (SC) current generated by the PM flux. However, the application of IPMSM in fault-tolerant areas has not yet been fully investigated. Additionally, the adoption of multi-phase or multiple 3-phase winding in PM machines offers enhanced redundancy and the potential for post fault-tolerant control without additional cost [11]. The dual 3-phase winding compromises the overall complexity and the fault-tolerant capability of the proposed machine. Moreover, the adoption of a dual 3-phase design can inherit power converters and control strategies from the conventional 3-phase design, while the winding redundancy can ensure continuous operation under fault conditions [12].

In this paper, a fault-tolerant IPMSM (FT-IPMSM) with dual 3-phase winding is designed for eVTOL application. The rest of the paper is arranged as follows. First, the design of FT-IPMSMs is introduced in Section II. Two dual 3-phase winding configurations are investigated, focusing on their influence on the fault-tolerant capability of the machine, including the conventional overlapped winding and segregated distributed winding. Additionally, Four different rotor topologies are discussed and proposed, i.e. the 1-layer V-shaped PM, 2-layer V-shaped PM, 3-layer V-shaped PM, and ∇-shaped PM. The initial topologies of four rotor designs are optimized, and the key performance of each design is compared in detail in Section III. In Section IV, the multi-physics performance of the optimal design and the fault-tolerant capability of the proposed two dual 3-phase windings are evaluated. Finally, the last section concludes the article.

II. MACHINE DESIGN

A. Dual 3-Phase Winding Design

The distributed windings have been employed in this article to suppress harmonics in the air-gap field, thereby improving the efficiency of the proposed machine. The conventional dual 3-phase winding configuration, denoted as W1#, is shown in Fig. 1(a). The phasor diagram shown in Fig. 1(c) indicates that two sets of 3-phase winding are required to be excited by currents out of phase of 30°. This winding configuration can enhance the output torque and restrict the torque ripple. However, it can be discovered that two sets of 3-phase winding are overlapped and bundled with each other. The physical connections between two winding sets and magnetic and thermal coupling facilitate fault propagation and may deteriorate its fault-tolerant capabilities.

To realize the effective physical, electrical, and thermal isolation between two winding sets, a segregated dual 3-phase winding has been proposed, denoted as W2#, as shown in Fig. 1(b). The conventional dual 3-phase winding has been rewound into four separated 3-phase modules without changing the current distribution in each slot. Each set of 3-phase winding is driven by an individual 3-phase inverter, thereby an effective physical, electrical, and thermal isolation between each winding set can be achieved. However, there is a slight reduction in the output torque of the machine under healthy conditions due to the 0° angle displacement between two sets of 3-phase winding, as shown in Fig. 1(d). In this condition, to reach a compromise between redundancy and complexity, the 48-slot/8-pole scheme has been chosen for the proposed FT-IPMSM.

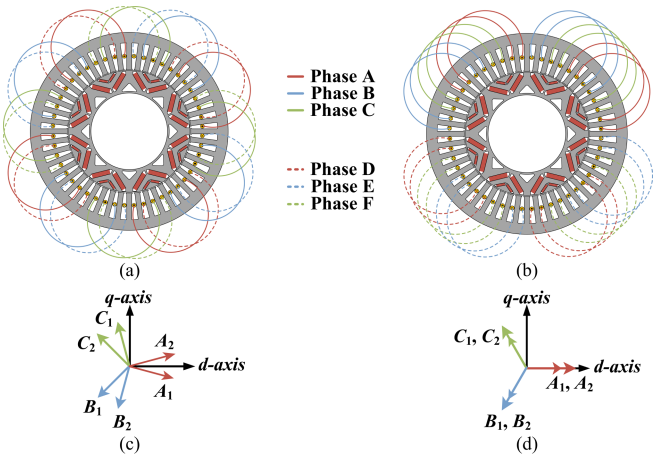

Fig. 1. Topologies and phasor diagrams of two dual 3-phase FT-IPMSM designs. (a) Conventional overlapped winding fed with current phase shifted by 30° (W1#), (b) Segregated distributed winding fed with current phase shifted by 0° (W2#), (c) Phasor diagram of W1#, (d) Phasor diagram of W2#.

B. Initial Topology Selection

The stator and rotor employ the cobalt-iron lamination Vacoflux 48 with 0.35mm width to improve the flux density and restrict the iron loss. The material for PM is chosen as N48EH, minimizing the influence of temperature on the operational performance of the prototype.

The proposed machine is required to operate across a wide rotational range from 3000r/min to 12000r/min. In this condition, the interior PM configuration has been adopted due to its field weakening capability and wide constant power speed range (CPSR) benefits. Moreover, the interior PM equipment method can exploit the reluctance torque to enhance the torque density due to the magnetic saliency of the rotor. In other words, the IPMSM can maintain the output capability with a reduction in PM consumption. It is critical for the machine to suppress the SC currents under the SC fault condition and enhance fault-tolerance.

The reluctance torque generated by the IPMSM can be influenced by rotor structures [15]. Therefore, four different PM configurations, i.e. 1-layer V-shaped PM, 2-layer V-shaped PM, 3-layer V-shaped PM, and ∇-shaped PM, are designed and their performance is compared in-depth. The initial topologies for four prototypes are shown in Fig. 2. It should be noted that the proposed four designs share the same stator topology, winding configuration, and PM materials. The next section will discuss the optimization method and give a trade study on the proposed four rotor topologies.

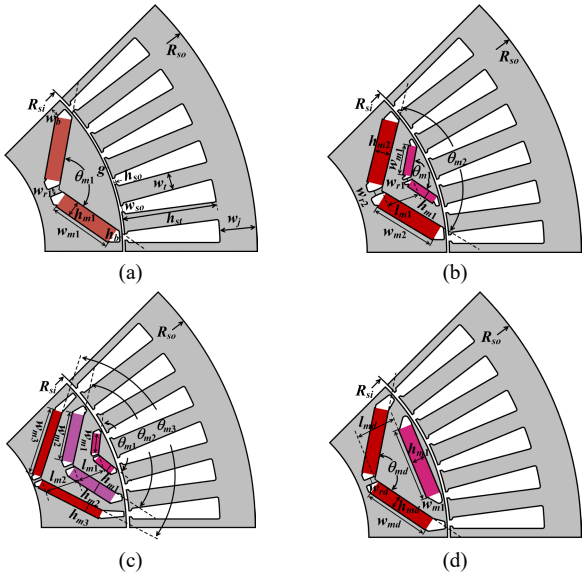

Fig. 2. Four IPMSM rotor topologies. (a) 1-layer V-shaped PM, (b) 2-layer V-shaped PM, (c) 3-layer V-shaped PM, (d) ∇-shaped PM.

III. DESIGN OPTIMIZATION AND COMPARISON

In this section, the initial design of the proposed IPMSM with four different rotor topologies will be optimized. The performance of optimized designs will be evaluated and compared in terms of torque density, efficiency, magnet usage, power factor, and fault-tolerant capability.

A. Optimization Objectives and Constraints

The multi-objective optimization algorithm has been implemented to achieve a comprehensive optimal design for four IPMSM prototypes. The optimization objectives for the proposed machine target to minimize the torque pulsation while maximizing efficiency as well as output torque or the PM utilization ratio, which is defined as the ratio of average torque to the PM volume. Furthermore, the terminal voltage must be constrained within the allowable limit of the power converter throughout the optimization process. As a result, the optimization objectives and constraints can be concluded as below

$$objectives: \begin{cases} max(Average\ Torque) \\ min(Torque\ Ripple) \\ max\left(\dfrac{Average\ Torque}{PM\ Volume}\right) \\ max\ Efficiency \end{cases} \quad (1)$$

$$s.t.\begin{cases} Peak\ Phase\ Terminal\ Voltage < 515V \\ hm_{1\times N} \in [2mm, 6mm] \end{cases} \quad (2)$$

B. Optimization Results and Discussion

The trade-off plots of four prototypes are shown in Fig. 3. The performance of four optimized designs is compared in terms of output torque, torque ripple, magnets volume, efficiency, power factor, and fault-tolerant capability. It can be discovered that the output torque requirement is attainable for all PM configurations while achieving an efficiency above 94%. Additionally, the torque ripple of the machine is distributed within the range of 10%-30%. Moreover, a PM utilization ratio exceeding 2.0kNm/L is achieved for all rotor designs except the 3-layer V-shaped PM configuration. For each PM configuration, the design that achieves a lower torque ripple, in addition to higher average torque, PM utilization ratio, and efficiency is selected as the optimal design.

Additionally, the fault-tolerant capability of the machine can be evaluated by the characteristic current I_{ch} as

$$I_{ch} = \psi_{PM}/L_d \quad (3)$$

where, ψ_{PM} is the PM flux, L_d is the d-axis inductance.

In (3), low PM flux ψ_{PM} and high d-axis inductance L_d will result in low characteristic current I_{ch} as well as low SC current. Therefore, the value of I_{ch} can be used to predict the performance of the prototype under short-circuit fault conditions.

Furthermore, the signal-to-noise ratio SN is adopted to evaluate the performance of four optimized rotor topologies as expressed in (4) and (5) [14]. It can be discovered that (4) is well-suited for objectives such as average torque, efficiency, and power factor. Higher values of these objectives indicate better machine performance. On the contrary, (5) is used to evaluate objectives, such as torque ripple and characteristics current, where lower values indicate better performance.

$$SN = -10\log_{10}(1/y^2) \quad (4)$$

$$SN = -10\log_{10}(y^2) \quad (5)$$

The SN results are normalized to give a reasonable comparison to different optimization objectives, as shown in (6).

$$\text{norm}(SN) = (SN - \overline{SN})/s.d(SN) \quad (6)$$

where, y is the result of optimization objectives, $\overline{SN}$ and $s.d(SN)$ are the average value and the standard deviation of SN, respectively.

Fig. 4 illustrates the comparison results of four FT-IPMSM designs. It can be discovered that the 2-layer V-shaped design outperforms the 3-layer V-shaped and ∇-shaped counterparts in almost all aspects except the power factor. Although the magnet volume and characteristic currents of the 2-layer V-shaped design are higher than that of the 1-layer V-shaped counterpart, the former exhibits a much larger average torque than the latter, meeting the optimization requirements. Therefore, the 2-layer V-shaped design is more satisfying and has been considered comprehensively. It has been selected to be investigated in the following section. The major parameters of the optimized machine are shown in TABLE I.

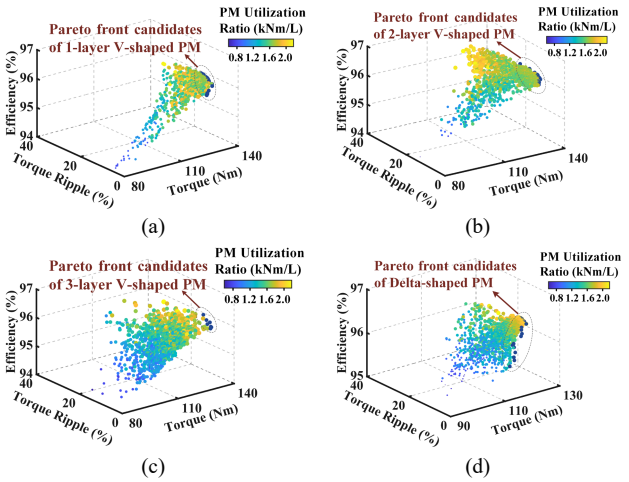

Fig. 3. Trade-off plots for different rotors. (a) 1-layer V-shaped PM, (b) 2-layer V-shaped PM, (c) 3-layer V-shaped PM, (d) ∇-shaped PM.

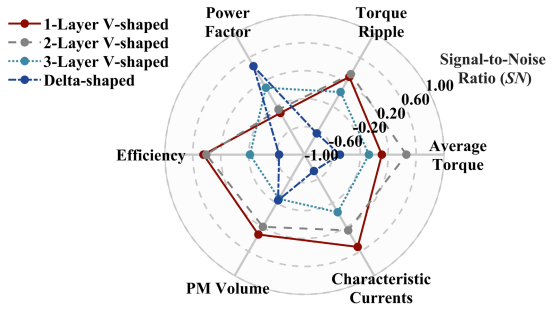

Fig. 4. Performance comparison of four optimized PM designs.

TABLE I. MAJOR PARAMETERS OF THE OPTIMIZED 2-LAYER V-SHAPED FT-IPMSM

	Parameter	Value
Structure Parameters	Slot/pole combination	48/8
	Stator outer radius, R_{so} (mm)	181.9
	Stator inner radius, R_{si} (mm)	113.2
	Rotor inner radius, R_{ri} (mm)	65
	Airgap length, g (mm)	0.73
Key Performance	Rated speed, n (r/min)	3000
	Rate torque, Nm	130
	Rated current, I_{rms} (A)	107.5
	Torque density, (Nm/kg)	15
	Power factor	0.92
	Efficiency, (%)	96

IV. PERFORMANCE EVALUATION

In this section, the multi-physics performance evaluation will be carried out for the optimized FT-IPMSM with the 2-layer V-shaped PM. The thermal and mechanical performance of the prototype will be evaluated based on finite element analysis (FEA). Finally, the fault-tolerant capability of the dual 3-phase overlapped winding and the segregated winding will be studied and compared in this section.

A. Thermal Performance

Due to the necessity of high-torque-density, an effective cooling system is critical for the proposed machine to ensure its thermal safety. In this study, the hybrid cooling system, which consists of water cooling and axial air cooling methods, has been applied to enhance the current density as well as the torque density of the machine. The schematic of the cooling system of the machine is shown in Fig. 5. The liquid cooling

with an axial Z-shaped water channel has been applied considering the easy manufacturing and uniform heat dissipation. Moreover, the forced air cooling system has been adopted to remove heat directly from the rotor and stator end-winding. In addition, epoxy has further been used as a passive cooling method to reduce the temperature of the end winding. In this study, The water jacket (WJ) is designed with a 30L/min flow and cooling water with 40°C inlet temperature has been used. In addition, the machine is also axial air-cooled with a flow rate of 1500L/min.

The thermal performance of the machine under the steady condition has been calculated based on the lumped parameter thermal network (LPTN). The temperature distribution of each part of the machine has been displayed in TABLE II. The calculation results indicate that the steady temperature of all components inside the machine is lower than the critical temperature. Therefore, the prototype can operate long-term without any thermal risks.

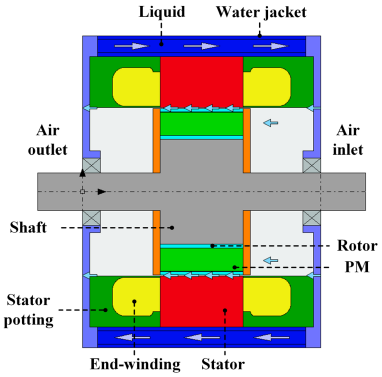

Fig. 5. Thermal system of the machine.

TABLE II. TEMPERATURES OF EACH PART OF THE MACHINE

Part	End-Winding Potting, °C	Critical Temperature, °C
Stator Lamination	69.5	-
Stator Surface	98.4	-
Magnet	67.1	**150**
Rotor Lamination	67.0	-
Rotor Surface	66.4	-
Winding	123.8	**180**
End Winding	140.8	**180**

TABLE III. MECHANICAL PROPERTIES OF THE ROTOR MATERIALS

Parameter	Materials	
	Vacoflux 48	Vacoflux 50
Mass density, kg/m^3	8120	8120
Young's moudulus, GPa	200	215
Poisson's ratio	0.3	0.3
Yield strength, MPa	200	390

B. *Mechanical Performance*

To guarantee the mechanical safety of the rotor under the maximum operating speed, the rotational speed is set to 10% higher than the maximum speed (13.2krpm) to provide a safety factor.

Fig. 6(a) shows the initial rotor design of the rotor structure in which the circular cavities are adopted to reduce the mass of the rotor further, thereby enhancing the torque density of the machine. The stress distribution of the initial design is shown in Fig. 6(a). The rotor stress is evenly distributed, with the maximum value occurring at the central rib in the second magnet row due to the mass of PMs, as shown in Fig. 7, highlighting a further optimization of the central rib structure. Meanwhile, the maximum rotor stress reaches about 231.02MPa, exceeding the allowable stress of Vacoflux 48, requiring a stronger material. To enhance the mechanical capability, the outline shape of the central rib in the second row has been updated from parallel faces to two curved faces, as shown in Fig. 6(b). Additionally, Vacoflux 50 is employed in place of Vacoflux 48 in the rotor, as it offers 1.8 times higher yield strength while maintaining comparable electrical performance, as shown in TABLE III. Fig. 6(b) shows the stress distribution in the optimized rotor topology. It can be discovered that the maximum stress in the rotor has reduced by about 16% to 193MPa, which is lower than the safety limit of the Vacoflux 50 with a yield strength of 390MPa.

It should be noted that the only change in the central rib is its outline shape. Therefore, this optimization will not increase the length of the bridge, ensuring that the flux leakage through the bridge remains almost unchanged. In this condition, the mechanical capability of the rotor can be improved without additional cost, while the electromagnetic performance of the machine, especially the output torque of the machine can be maintained.

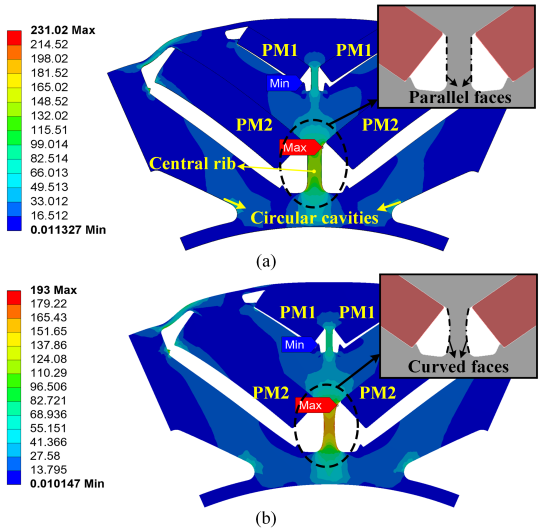

Fig. 6. Von-Mises stress of the rotor at 13.2krpm. (a) Initial rotor design, (b) Optimized rotor design.

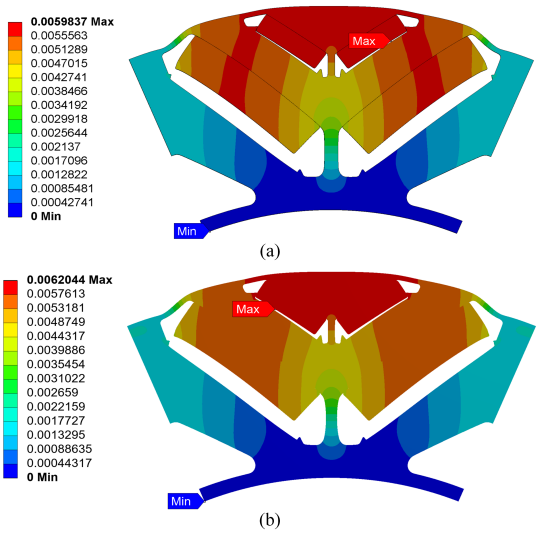

Fig. 7. Total deformation of the optimized rotor at 13.2krpm. (a) Initial rotor design, (b) Optimized rotor design.

C. Fault-Tolerant Performance

This section conducts a comparison of the fault-tolerant performance of the proposed machine with W1# and W2# under the one-set open-circuit (OC) fault condition and the one-set SC fault condition. To simplify the analysis, all evaluations are conducted when the fault happens in the ABC set without otherwise mentioned. In this condition, the inverter of the faulty set (ABC set) will be deactivated while the healthy set (DEF set) still excited by 3-phase currents.

1) *One-Set Open-Circuit (OC) Fault Condition:*

According to the aforementioned analysis, the inverter of the ABC set has been cut off when the fault happens, while the DEF set remains in operation. The resultant OC torque and spectrums are shown in Fig. 8. It can be observed that the output torque of both W1# and W2# has decreased to about half of that in the healthy case, while the torque of W2# is slightly higher than W1#. Furthermore, W2# shows a significant $6f_e$ and $12f_e$ (f_e is electrical frequency) torque ripple component, while W1# is predominantly characterized by the $6f_e$ torque ripple component. As shown in Fig. 8(b), there is a $2f_e$ fluctuation component in the spectrum of W2#, which has not been observed in W1#. The $2f_e$ fluctuation component in W2# can be attributed to the periodic iron saturation caused by the offset component in the armature magnetomotive force (MMF).

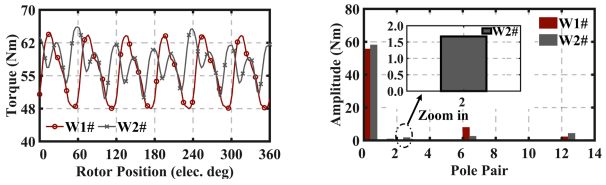

(a) (b)

Fig. 8. OC torque comparions. (a) OC torque waveforms, (b) OC torque spectrums.

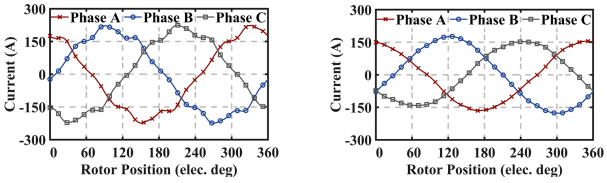

(a) (b)

Fig. 9. SC currents comparisons. (a) W1#, (b) W2#.

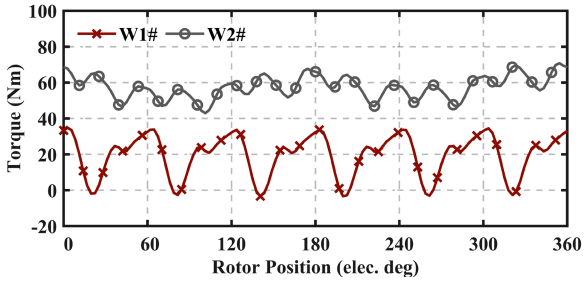

Fig. 10. SC torque comparisons.

2) *One-Set Short-Circuit (SC) Fault Condition:*

When the SC fault happens, the terminals of the faulty winding should be short-circuited to form a terminal short-circuit (TSC). The corresponding SC currents can counteract the residual flux coupled by the ABC set, thereby restricting SC currents. The SC currents in the ABC set when TSC applied are plotted in Fig. 9. In SC cases, the 3-phase SC currents can no longer remain symmetry, with the rms value of phase B is always higher than that of phase A and phase C for both W1# and W2#. As shown in Fig. 9, the SC currents of W1# are about 1.46p.u., which is higher than W2# with 1.15p.u. Additionally, more SC current harmonics are observed in W1# and its total harmonic distortion (THD) is about 0.036%, which is about 2 times higher than that of W2# (0.019%), indicating a weaker harmonic suppression of W1#. The high SC currents and poor harmonic suppression capability can be attributed to the lower self-inductance in W1#, aligned with its relatively higher PM flux.

Fig. 10 shows the resultant torque under the SC condition. It is shown that the torque of W1# is almost zero due to the strong coupling between two sets of 3-phase winding. In comparison, W2# exhibits a much higher torque than W1#, reaching around 58Nm.

V. Conclusion

This article developed a dual 3-phase 48-slot/8-pole FT-IPMSM for eVTOL applications. Four typical rotor topologies have been proposed and optimized with considerations of output performance and fault-tolerant capability, including the 1-layer V-shaped PM, 2-layer V-shaped PM, 3-layer V-shaped PM, and ∇-shaped PM. The optimization results reveal that the 2-layer V-shaped PM offers higher output torque, efficiency, power factor, and PM utilization ratio while exhibiting lower characteristic currents, making it the preferred choice for further investigation. The multi-physics analysis has further demonstrated that the machine can operate continuously without any thermal or mechanical risks. Furthermore, it confirms that the maximum stress in the rotor is reduced by about 16% by properly optimizing the rotor structure. Finally, the fault-tolerant capability of the prototype is assessed with different winding configurations, proving that the segregated dual 3-phase winding can enhance the fault-tolerant capability.

Acknowledgment

This work was supported by Shenzhen Science and Technology Program under Grant GJHZ20240218114402006, and in part by Royal Society under Grant RG\R1\251550.

References

[1] C. Wenping, B. C. Mecrow, G. J. Atkinson, J. W. Bennett, and D. J. Atkinson, "Overview of Electric Motor Technologies Used for More Electric Aircraft (MEA)," *IEEE Trans. Ind. Electron.*, vol. 59, no. 9, pp. 3523-3531, Sept. 2012.

[2] Y. Wang, S. Nuzzo, H. Zhang, W. Zhao, C. Gerada, and M. Galea, "Challenges and Opportunities for Wound Field Synchronous Generators in Future More Electric Aircraft," *IEEE Trans. Transp. Electrif.*, vol. 6, no. 4, pp. 1466-1477, Dec. 2020.

[3] N. Dave et al., "Fast Sizing Tool and Optimization Technique for Concentrated Wound Slotless Outer Rotor Motor for eVTOL Application," *2022 International Conference on Electrical Machines (ICEM)*, Valencia, Spain, 2022, pp. 2094-2099.

[4] B. Sarlioglu and C. T. Morris, "More Electric Aircraft: Review, Challenges, and Opportunities for Commercial Transport Aircraft," *IEEE Trans. Transp. Electrif.*, vol. 1, no. 1, pp. 54-64, June 2015.

[5] E. Sayed et al., "Review of Electric Machines in More-/Hybrid-/Turbo-Electric Aircraft," *IEEE Trans. Transp. Electrif.*, vol. 7, no. 4, pp. 2976-3005, Dec. 2021.

[6] Z. Q. Zhu and D. Howe, "Electrical Machines and Drives for Electric, Hybrid, and Fuel Cell Vehicles," *Proc. IEEE*, vol. 95, no. 4, pp. 746-765, April 2007.

[7] Q. Chen, G. Liu, W. Zhao, L. Sun, M. Shao and Z. Liu, "Design and Comparison of Two Fault-Tolerant Interior-Permanent-Magnet Motors," *IEEE Trans. Ind. Electron.*, vol. 61, no. 12, pp. 6615-6623, Dec. 2014.

[8] G. Pellegrino, A. Vagati, P. Guglielmi and B. Boazzo, "Performance Comparison Between Surface-Mounted and Interior PM Motor Drives for Electric Vehicle Application," *IEEE Trans. Ind. Electron.*, vol. 59, no. 2, pp. 803-811, Feb. 2012.

[9] S. Wu, D. D. Reigosa, Y. Shibukawa, M. A. Leetmaa, R. D. Lorenz and Y. Li, "Interior Permanent-Magnet Synchronous Motor Design for Improving Self-Sensing Performance at Very Low Speed," *IEEE Trans. Ind. Appl.*, vol. 45, no. 6, pp. 1939-1946, Nov.-dec. 2009.

[10] K. Yamazaki and M. Kumagai, "Torque Analysis of Interior Permanent-Magnet Synchronous Motors by Considering Cross-Magnetization: Variation in Torque Components With Permanent-Magnet Configurations," *IEEE Trans. Ind. Electron.*, vol. 61, no. 7, pp. 3192-3201, July 2014.

[11] N. Bianchi, S. Bolognani and M. D. PrÉDai Pre, "Impact of Stator Winding of a Five-Phase Permanent-Magnet Motor on Postfault Operations," *IEEE Trans. Ind. Electron.*, vol. 55, no. 5, pp. 1978-1987, May 2008.

[12] M. Barcaro, N. Bianchi and F. Magnussen, "Six-Phase Supply Feasibility Using a PM Fractional-Slot Dual Winding Machine," *IEEE Trans. Ind. Appl.*, vol. 47, no. 5, pp. 2042-2050, Sept.-Oct. 2011.

[13] H. Chen and C. H. T. Lee, "Parametric Sensitivity Analysis and Design Optimization of an Interior Permanent Magnet Synchronous Motor," *IEEE Access*, vol. 7, pp. 159918-159929, 2019.

[14] D. -K. Lim, K. -P. Yi, S. -Y. Jung, H. -K. Jung and J. Ro, "Optimal Design of an Interior Permanent Magnet Synchronous Motor by Using a New Surrogate-Assisted Multi-Objective Optimization," *IEEE Trans. Magn.*, vol. 51, no. 11, pp. 1-4, Nov. 2015.

[15] X. Liu, H. Chen, J. Zhao and A. Belahcen, "Research on the Performances and Parameters of Interior PMSM Used for Electric Vehicles," *IEEE Trans. Ind. Electron.*, vol. 63, no. 6, pp. 3533-3545, June 2016.